Low-Temperature Structure and Magnetic Properties of the Spinel $LiMn_2O_4$: A Frustrated Antiferromagnet and Cathode Material

A. S. Wills, N. P. Raju, and J. E. Greedan*

Brockhouse Institute for Materials Research, McMaster University, 1280 Main Street West, Hamilton, Ontario, Canada, L8S 4M1

Received November 2, 1998. Revised Manuscript Received March 24, 1999

Powder neutron diffraction has been used to study the nature of the structural transition away from the *Fd*3*m* cubic structure upon cooling below ∼285 K in the spinel $LiMn_2O_4$. We report powder data taken between 10 K and 333 K and propose a large cell tetragonal structure in space group $I4_1/amd$ for the material at 100 K. While complete segregation of the Mn^{3+} and Mn^{4+} ions is not possible in this space group, bond-valence analysis indicates that the distribution of Mn^{3+} and Mn^{4+} ions is not random and that there is a degree of charge segregation. Further, $LiMn_2O_4$ is also of interest because it is an example of a geometrically frustrated antiferromagnet. Direct current magnetic susceptibility measurements show field-cooled, zero-field-cooled irreversibility at ∼65 K and a maximum in zero-field-cooled data at ∼40 K. Neutron diffraction shows magnetic scattering in the form of a broad peak assigned to short-range order which develops above 100 K. Upon cooling to 60 K additional Bragg peaks are seen, signaling long-range magnetic order. The Bragg peaks grow at the expense of the diffuse feature on cooling to 10 K but the latter persists even at the lowest temperature studied which indicates that a significant fraction of the spins still remain disordered. The magnetic Bragg peaks index on a tetragonal cell which is 2a, 2b, and 4c with respect to the low-temperature tetragonal cell and contains 1152 spins. The large size and implied complexity of the magnetic structure is consistent with both charge segregation and significant further neighbor exchange interactions.

1. Introduction

$LiMn_2O_4$ has found important applications as a cathode material in secondary lithium ion batteries.[1−5] Despite the intense interest in this material by the electrochemical community there exist few reported studies of the interesting structural and magnetic phase transitions.[6,7] Above a Verwey transition at ∼285 K its crystal structure is cubic and is described in space group *Fd*3*m* (Figure 1). The oxygen atoms form a cubic-close-packed array in which the Li and Mn ions reside at tetrahedral (8a) and octahedral (16d) sites, respectively. With an average manganese valency, *v*(Mn), of 3.5, the manganese formally exists in Mn^{4+} ($t_{2g}^3e_g^0$) and Jahn−Teller active Mn^{3+} ($t_{2g}^3e_g^1$) configurations. However, unlike the structurally related mixed-valent perovskites where the 180° Mn−O−Mn interactions are sufficiently strong to lead to itinerant e_g electrons, the 90° bridging arrangement in the spinel structure causes e_g orbitals on neighboring Mn atoms to be orthogonal and the e_g electrons to be localized and correspondingly, $LiMn_2O_4$ shows no metallic behavior at room temperature. Instead it is a semiconductor[8−10] (at room temperature the conductivity $\sigma \approx 10^{-4}$ S/cm) where a dynamic Jahn−Teller distortion in the environment around Mn^{3+} is apparently sufficient to retard the motion of the e_g electrons, but averaged over time does not lead to reduction in the symmetry of the lattice away from the space group *Fd*3*m*. Indeed, in this regime thermopower experiments show that $LiMn_2O_4$ is a small polaron conductor.[9] The presence of a Verwey transition suggests that the e_g electrons become at least partially localized with distinguishable Mn^{3+} and Mn^{4+} cations and environments, consistent with the observed distortion away from cubic symmetry. Previous work has suggested that the low-temperature structure is a simple tetragonal variant of the *Fd*3*m* structure,[7] or has a large orthorhombic cell.[6] DSC measurements indicate that the structural transition is first order which leads to hysteresis upon cooling and then heating to room temperature.[7,10,11]

(1) Thackeray, M. M.; Dekock, A.; Rossouw, M. H.; Liles, D.; Bittihn, R.; Hoge, D. *J. Electrochem. Soc.* **1992**, *139*, 363.
(2) Thackeray, M. M. *J. Electrochem. Soc.* **1995**, *142*, 2558.
(3) Bruce, P. G. *Philos. Trans. R. Soc. London Ser. A* **1996**, *354*, 1577.
(4) Goodenough, J. B. *Solid State Ionics* **1994**, *69*, 184.
(5) Guyomard, D.; Tarascon, J. M. *Solid State Ionics* **1994**, *69*, 222.
(6) Rodriguez-Carvajal, J.; Rousse, G.; Masquelier, C.; Hervieu, M. *Phys. Rev. Lett.* **1998**, in press.
(7) Yamada, A.; Tanaka, M. *Mater. Res. Bull.* **1995**, *30*, 715.
(8) Shimakawa, Y.; Numata, T.; Tabuchi, J. J. *Solid State Chem.* **1997**, *131*, 138.
(9) Massarotti, V.; Capsoni, D.; Bini, M.; Chiodelli, G.; Azzoni, C. B.; Mozzati, M. C.; Paleari, A. *J. Solid State Chem.* **1997**, *131*, 94.
(10) Sugiyama, J.; Atsumi, T.; Koiwai, A.; Sasaki, T.; Hioki, T.; Noda, S.; Kamegashira, N. *J. Phys.*: *Condens. Matter* **1997**, *9*, 1729.
(11) Masquelier, C.; Tabuchi, M.; Ado, K.; Kanno, R.; Kobayashi, Y.; Maki, Y.; Nakamura, O.; Goodenough, J. B. *J. Solid State Chem.* **1996**, *123*, 255.

10.1021/cm981041l CCC: $18.00
Published on Web 05/15/1999

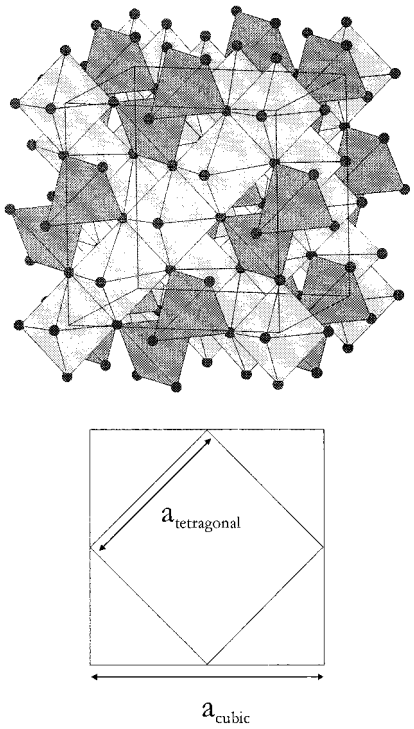

Figure 1. Polyhedral representation of the cubic room-temperature structure of $LiMn_2O_4$ and the relation between cubic and tetragonal unit cells.

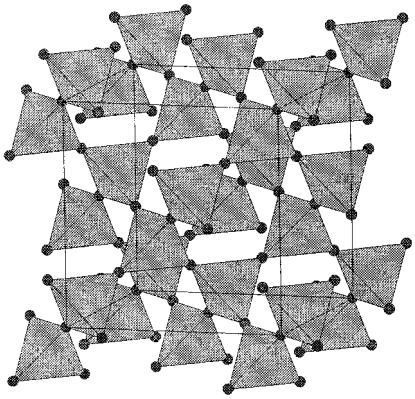

Figure 2. The pyrochlore lattice made up of vertex-sharing tetrahedra.

In addition to these structural issues, the magnetic properties of $LiMn_2O_4$ are worthy of study as the magnetic sublattice consists of a network of vertex sharing tetrahedra known also as the *pyrochlore* network (Figure 2). Antiferromagnets which have this connectivity are described as being frustrated[12,13] because four moments at the vertexes of a tetrahedron cannot align themselves in such a way as to be simultaneously antiparallel to each other (Figure 3a), and the tendency for neighboring moments to align antiferromagnetically causes them to adopt a canted configuration in which the vector sum of the moments over a tetrahedron is zero (Figure 3b). The pyrochlore framework represents a particularly special geometry because, given the criterion of the vector sum of moments on each tetrahedron being zero, the connectivity of sharing only one vertex between tetrahedra is insufficient to define a unique spin structure. This leads to the system having a large number of degenerate lowest energy spin configurations and a corresponding difficulty in the selection of an unique ground state.[14] In materials based on the pyrochlore mineral structure the magnetic exchange system can be closely approximated by nearest-neighbor exchange and these systems possess a highly degenerate ground-state manifold.[15] In the cubic spinels however, the geometry of the crystal structure allows further neighbor interactions that are of comparable strength to those of the nearest neighbor. This breaks the degeneracy of the ground-state manifold and leads to the selection of particular magnetic structures. Which structure is chosen depends on the precise balance between the various exchange pathways in the system. In the case of the isomorphic spinel λ-MnO_2, which is formed by de-insertion of lithium from $LiMn_2O_4$, the low-temperature magnetic structure has different moment patterns of local Mn tetrahedra that cannot be explained on the basis of nearest-neighbor exchange.[16]

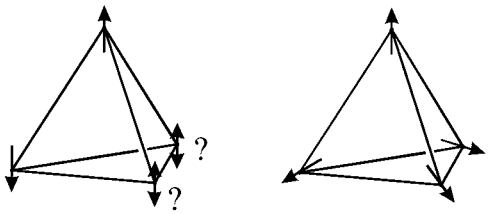

Figure 3. (a) A frustrated arrangement of spins on a tetrahedron and (b) the compromise arrangement of canted moments at 109° to each other.

Previous literature also holds the conflicting reports of an antiferromagnetic transition observed in the ^7Li NMR[10,17] but not in the dc susceptibility.[8,18] We examined the magnetic properties of $LiMn_2O_4$ using a combination of dc susceptibility and neutron powder diffraction.

2. Experimental Section

2.1. Preparation. Preparation of two samples of $LiMn_2O_4$ were done using standard solid-state techniques: Li_2CO_3 (J. T. Baker Chemical Co., 99.1%) and Mn_2O_3 (Alfa Inorganics, Ventron, 98%) were thoroughly ground under acetone and the dried mixture was pelletized. The pellets were prefired in air at 650 °C for 12 h before being heated to 800 °C. They were held at this temperature for 24 h and then cooled to room temperature. To improve homogeneity the product was ground, repelletized, and again fired at 800 °C.

2.2. Direct Current Susceptibility. Direct current susceptibility measurements were taken using a Quantum Design MPMS SQUID magnetometer between 2 and 500 K. Data were taken with the samples cooled in a number of measuring fields between 10 and 50 000 Oe with the sample cooled in the absence of an applied field (zero-field cooled) and in the measuring field (field-cooled).

2.3. DSC. DSC analyses were performed using a TA instruments DSC 2910. The samples were held in aluminum pans and heated and cooled under N_2 gas. The heating/cooling rate was 15 °C/min. The heat−cool cycle was between −30 to 50 °C and back to −30 °C.

(12) Anderson, P. W. *Phys. Rev.* **1956**, *102*, 1008.
(13) Villain, J. *Z. Phys. B* **1979**, *33*, 31.
(14) Reimers, J. N. *Phys. Rev. B*: *Condens. Matter* **1992**, *45*, 7287.
(15) Reimers, J. N.; Greedan, J. E.; Kremer, R. K.; Gmelin, E.; Subramanian, M. A. *Phys. Rev. B* **1991**, *43*, 3387.
(16) Greedan, J. E.; Raju, N. P.; Wills, A. S.; Morin, C.; Shaw, S. M.; Reimers, J. N. *Chem. Mater.* **1998**, *10*, 3058.
(17) Sugiyama, J.; Hioki, T.; Noda, S.; Kontani, M. *J. Phys. Soc. Jpn.* **1997**, *66*, 1187.
(18) Blasse, G. *J. Phys. Chem. Solids* **1966**, *27*, 383.

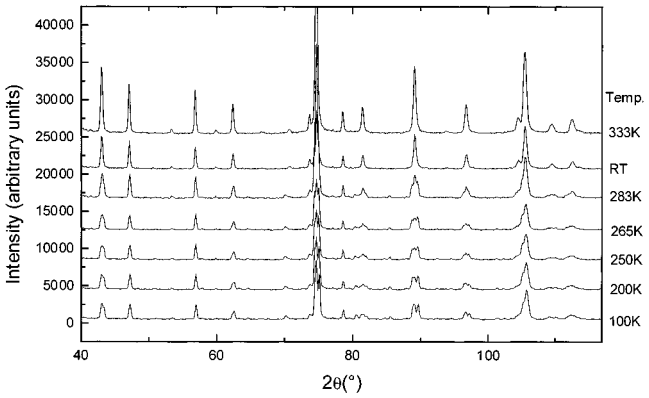

Figure 4. Powder neutron diffraction patterns of sample B of $LiMn_2O_4$ taken between 100 and 333 K with neutrons of wavelength 1.5030 Å.

2.4. Neutron Diffraction. Neutron diffraction data were taken using the high-resolution C2 diffractometer of the DUALSPEC facility at AECL, Chalk River Laboratories. To examine the question of whether the low-temperature cell is orthorhombic or tetragonal, data were collected at wavelengths of 1.3282 and 2.3713 Å at 100 K out to a momentum transfer of $q = 8.0$ and 4.49 $Å^{-1}$, respectively. Simultaneous refinement of the two data sets from sample A would provide both high effective resolution data on the peak overlap and the information at high angles required for complete structural analysis. Previous data taken from sample B using a wavelength of 1.5030 Å up to $q = 6.85$ $Å^{-1}$ gave information on the temperature dependence of the structural phase transition at temperatures between 10 and 333 K. Rietveld refinement was carried out using version 6 of the PC translation of the GSAS suite[19] and bond-valence analysis calculations performed using VaList.[20] Corrections to the thermal parameters due to absorption by the sample were made using the method of Hewat.[21,22]

3. Results

Below the Verwey transition, T_v, the e_g electrons are at least partially localized and there are distinguishable Mn^{3+} and Mn^{4+}cations and environments. Correspondingly, upon cooling below $T_v \sim 290$ K powder neutron diffraction reveals a progressive structural distortion away from the cubic $Fd3m$ structure observed at room temperature (Figure 4). It is useful to examine the transition in terms of an alternative tetragonal description of this cell (Figure 1) that can be constructed in space group $I4_1/amd$ with the tetragonal and cubic axes related by

$$a_{\text{tetragonal}} = b_{\text{tetragonal}} = \frac{a_{\text{cubic}}}{\sqrt{2}} \quad (1)$$

and

$$c_{\text{tetragonal}} = c_{\text{cubic}} \quad (2)$$

This unit cell therefore has half the volume of that with cubic symmetry. Previous low-temperature X-ray diffraction data taken from a single crystal of lithium manganate grown from a flux indicated that the distortion away from the cubic structure corresponds again to a tetragonal cell which retains the $I4_1/amd$ symmetry, however, with a tripling of the a and b axes.[23] While such a distortion appears unusual, with the retention of space group symmetry the two cells are isomorphic. The positions of the manganese atoms were determined by direct methods and the remaining atoms located from difference Fourier maps. Severe twinning however prevented the refinement of accurate structural parameters and these were instead determined using powder neutron diffraction.

We find that at 100 K this tetragonal structure does indeed fit the powder neutron powder diffraction data and no evidence is seen of a distortion to lower symmetry such as orthorhombic as suggested by Rodriguez-Carvajal et al.[6] Indeed, fits to our own data using their model did not yield significant improvements to the agreement indices. The model proposed here is, apart from the different symmetry, a subcell of that of Rodriguez-Carvajal et al.[6] However, the large size of the unit cell and the complexity of the relationship between structural properties and precise sample stoichiometry prevents the exclusion of this possibility for all $Li_{1\pm x}Mn_2O_4$ samples. The difference Fourier maps showed no evidence for Li segregation leading to movement of Li onto octahedral sites and the structural details of the $I4_1/amd$ cell at 100 K refined for sample A are given in Table 1. Atoms with the same atomic number were constrained to have identical thermal parameters. Allowing fractional occupancies of the sites to vary did not improve the quality of the refinement and all values were set to unity. The refined profiles for sample A are shown in Figures 5 and 6. In addition to the reflections of the $I4_1/amd$ structure the data sets collected from sample A have an additional impurity peak observed at $d = 2.3$ Å (Figure 7). This peak does not disappear above the Verwey temperature and appears to correspond to the (2 2 2) reflection of a separate lithium-depleted λ-MnO_2 phase ($a_0 = 8.05$ Å). Such a phase was introduced into the calculations and its proportion refined to ~4 wt %. No additional data are reported on this second phase as only a single reflection and no temperature-dependent responses characteristic of λ-MnO_2 were observed in susceptibility or diffraction data. The refined structure of sample B at 100 K was consistent with that from the sample A and showed no contributions from the λ-MnO_2 impurity phase (Figure 8). The smaller dataset did not allow stable refinement of independent thermal parameters. However, stability was achieved by constraining all thermal parameters to be the same. Structural parameters for sample B are given in Table 2.

While the multiplicities of the Mn sites within the $I4_1/amd$ cell prevents complete segregation of the two Mn valencies, bond-valence analysis of the different Mn environments suggests that the distribution of Mn^{3+} and Mn^{4+} ions within the unit cell is not random and that there is indeed segregation of the Mn^{3+} and Mn^{4+} ions. The bond valences, s_{ij}, were calculated with the formula:

$$\sum_{ij} s_{ij} = \sum_{ij} \exp[(d_0 - d_{ij})/0.37]) \quad (3)$$

(19) von Dreele, R. B.; Larson, A. C. General Structure Analysis System, 1997. Software available from http://strider.lansce.lanl.gov/mlnsc/gsas/.

(20) Wills, A. S.; Brown, I. D. *VaList*; CEA: France 1999. Program available from author at willsas@netscape.net.

(21) Hewat, H. *Acta Crystallogr.* **1979**, *A35*, 248.

(22) Rouse, K. D.; Cooper M. J. *Acta Crystallogr.* **1970**, *A26*, 682.

(23) Dabkowska, H. A.; Britten, J. Unpublished work, 1997.

Table 1. Structural Parameters for $LiMn_2O_4$, Sample A, at 100 K in Space Group $I4_1/amd$ with $Z = 36$[a]

atom	*x*	*y*	*z*	U_{iso}, Å^2	site symmetry	Wyckoff site and multiplicity
Li1	0.500 0	0.750 0	0.375 0	0.001 41(34)	−4M2 001	4a
Li2	0.500 0	0.920 1(27)	0.65 7(4)	0.001 41(34)	M(100)	16h
Li3	0.167 9(18)	0.417 9(18)	0.375 0	0.001 41(34)	2(110)	16g
Mn4	0.250 0	0.574 7(14)	0.250 0	0.001 31(12)	2(010)	16f
Mn5	0.334 9(10)	0.675 1(8)	0.508 1(24)	0.001 31(12)	1	32i
Mn6	0.418 8(17)	0.750 0	0.738 3(47)	0.001 31(12)	M(010)	16h
Mn7	0.250 0	0.750 0	0.750 0	0.001 31(12)	2/M(010)	8d
O8	0.248 7(11)	0.750 0	0.526 2(23)	0.020 8(6)	M(010)	16h
O9	0.152 9(8)	0.511 3(6)	0.235 9(15)	0.020 8(6)	1	32i
O10	0.337 7(9)	0.680 4(6)	0.744 5(20)	0.020 8(6)	1	32i
O11	0.168 4(9)	0.659 6(6)	0.233 2(16)	0.020 8(6)	1	32i
O12	0.410 8(9)	0.750 0	0.510 7(28)	0.020 8(6)	M(010)	16h
O13	0.500 0	0.826 7(9)	0.756 7(27)	0.020 8(6)	M(100)	16h

[a] Cell parameters: $a = b = 17.5171(9)$ and $c = 8.1980(5)$. $\chi^2 = 10.30$. $R_{wp} = 10.71\%$, 9.41%, and 9.70% for 2.3713 Å, 1.3282 Å, and combined data sets respectively for 43 variables. Total number of profile points = 1618.

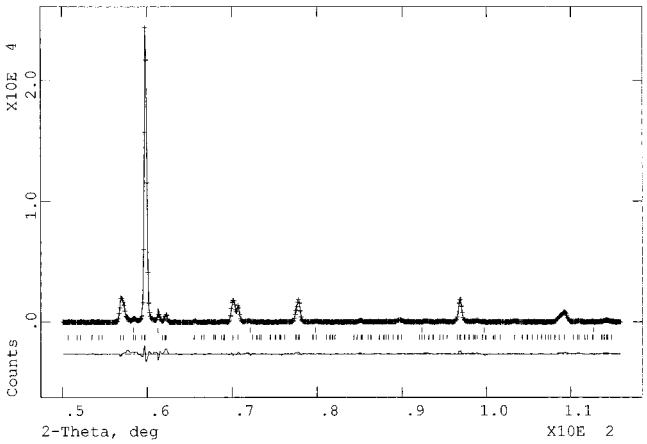

Figure 5. Fit of refined profile to neutron powder diffraction pattern from sample A of $LiMn_2O_4$ taken at 100 K with neutrons of wavelength 2.3713 Å. Upper ticks correspond to the λ-MnO_2 phase.

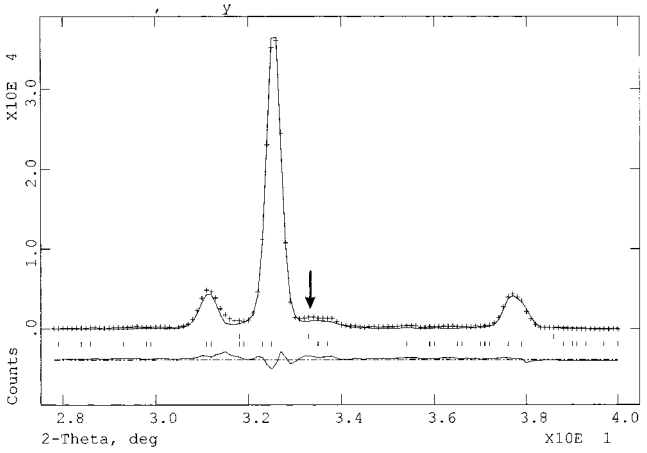

Figure 7. Close up of neutron powder diffraction pattern from sample A of $LiMn_2O_4$ taken at 100 K with neutrons of wavelength 2.3713 Å. The contribution from an impurity cubic λ-MnO_2 phase is indicated.

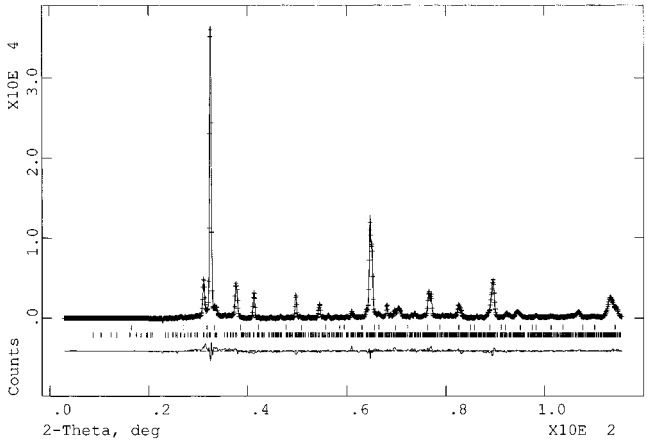

Figure 6. Fit of refined profile to neutron powder diffraction pattern from sample A of $LiMn_2O_4$ taken at 100 K with neutrons of wavelength 1.3282 Å. Upper ticks correspond to the λ-MnO_2 phase.

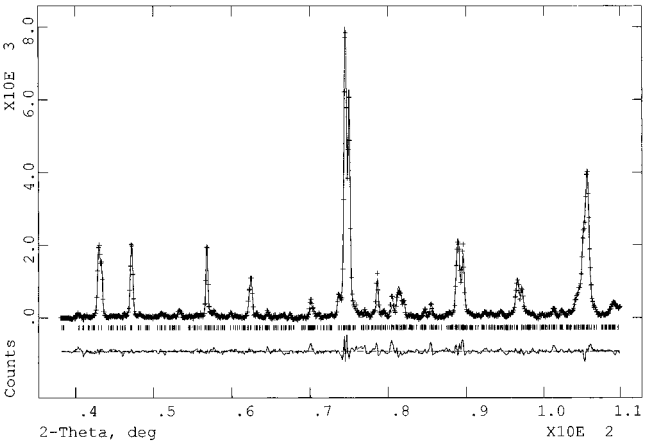

Figure 8. Fit of refined profile to neutron powder diffraction pattern from sample B of $LiMn_2O_4$ taken at 100 K with neutrons of wavelength 1.5030 Å.

where, d_{ij} is the bond length and d_0 a distance characterizing the cation−anion bond, d_0 (Mn^{3+}−O^{2-}) = 1.760, d_0(Mn^{4+}−O^{2-}) = 1.753.[24] The sum is over the bonded atoms *i* and *j*, and is made on the assumption of Mn being in the third and then separately in the fourth oxidation states. The balance of the Mn^{3+} and Mn^{4+} ratio is found to depend on the Mn site. In the case of the higher symmetry 8d site, bond-valence analysis indicates that the occupation is almost entirely by Mn^{4+}, while the Mn^{4+} content of the other sites is found to decrease with reduction in site symmetry. That is to say, as the proportion of Jahn−Teller active Mn^{3+} on a site increases there is a corresponding drop in the local symmetry of that site. The distribution of Mn^{3+} and

(24) Brese, N. E.; O'Keefe, M. *Acta Crystallogr.* **1991**, *B47*, 192.

Table 2. Structural Parameters for $LiMn_2O_4$, Sample B, at 100 K in Space Group $I4_1/amd$ with $Z = 36$[a]

atom	*x*	*y*	*z*	U_{iso}, Å^2	site symmetry	Wyckoff site and multiplicity
Li1	0.500 0	0.750 0	0.375 0	0.005 5(6)	−4M2 001	4a
Li2	0.500 0	0.908 4(23)	0.595(4)	0.005 5(6)	M(100)	16h
Li3	0.162 5(22)	0.412 5(22)	0.375 0	0.005 5(6)	2(110)	16g
Mn4	0.250 0	0.588 9(12)	0.250 0	0.005 5(6)	2(010)	16f
Mn5	0.337 0(11)	0.666 8(11)	0.499 9(32)	0.005 5(6)	1	32i
Mn6	0.415 5(14)	0.750 0	0.752 4(47)	0.005 5(6)	M(010)	16h
Mn7	0.250 0	0.750 0	0.750 0	0.005 5(6)	2/M(010)	8d
O8	0.249 4(11)	0.750 0	0.516 7(23)	0.005 5(6)	M(010)	16h
O9	0.151 3(8)	0.515 6(7)	0.227 9(16)	0.005 5(6)	1	32i
O10	0.334 5(8)	0.678 6(6)	0.735 8(18)	0.005 5(6)	1	32i
O11	0.170 7(8)	0.657 4(6)	0.238 8(19)	0.005 5(6)	1	32i
O12	0.411 5(9)	0.750 0	0.499 4(30)	0.005 5(6)	M(010)	16h
O13	0.500 0	0.830 0(9)	0.756 7(31)	0.005 5(6)	M(100)	16h

[a] Cell parameters: $a = b = 17.5402(5)$ and $c = 8.20515(28)$. $\chi^2 = 4.577$. $R_{wp} = 7.24\%$ for 34 variables. Total number of profile points = 709.

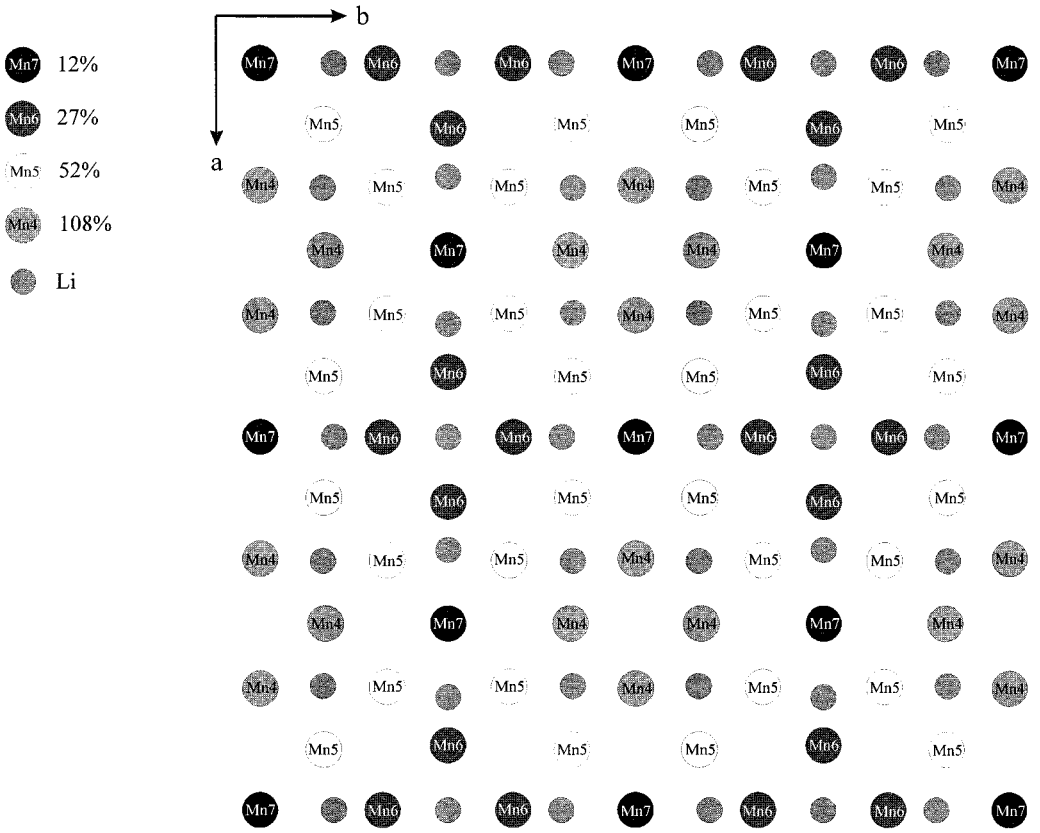

Figure 9. Projection in the *ab* plane indicating the distribution of Mn and Li atoms for sample A. The percentage occupation of Mn^{3+} on each site is shown.

Table 3. Bond-Valence Parameters for Sample A of $LiMn_2O_4$ at 100 K

atom name	⟨*d*(Mn−O)⟩, Å	$\sum_{ij} s_{ij}(Mn^{3+})$	$\sum_{ij} s_{ij}(Mn^{4+})$	%(Mn^{3+})	%(Mn^{4+})
Mn4	2.028	2.92	2.87	108	−8
Mn5	1.967	3.51	3.44	52	48
Mn6	1.938	3.78	3.71	27	73
Mn7	1.920	3.94	3.87	12	88

Table 4. Bond-Valence Parameters for Sample B of $LiMn_2O_4$ at 100 K

atom name	⟨*d*(Mn−O)⟩, Å	$\sum_{ij} s_{ij}(Mn^{3+})$	$\sum_{ij} s_{ij}(Mn^{4+})$	%(Mn^{3+})	%(Mn^{4+})
Mn4	1.967	3.66	3.59	38	62
Mn5	1.952	3.75	3.68	30	70
Mn6	1.990	3.28	3.22	73	27
Mn7	1.935	3.74	3.67	31	69

Mn^{4+} within the tetragonal unit cell is shown in projection in Figure 9.

The percentage of each Mn oxidation state present at a site is presented in Tables 3 and 4, which was calculated from the bond-valence sums for each oxidation state using the equations:

$$n_3 + n_4 = 1 \quad (4)$$

and

$$3n_3 + 4n_4 = n_3\sum_{ij} s_{ij}(Mn^{3+}) + n_4\sum_{ij} s_{ij}(Mn^{4+}) \quad (5)$$

Equation 4 constrains the total occupation of each site to be unity and eq 5 ensures that the oxidation state is given by the weighted bond-valence sum.

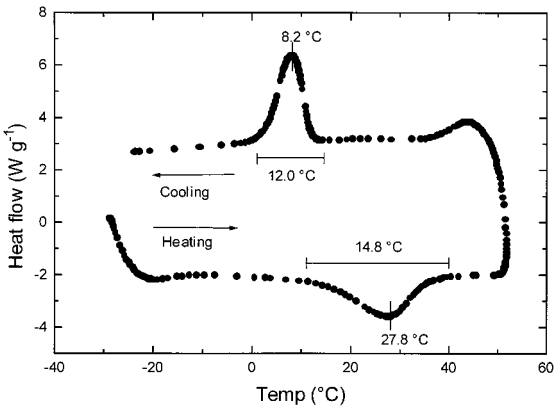

Figure 10. Differential scanning calorimetry traces for $LiMn_2O_4$, sample A.

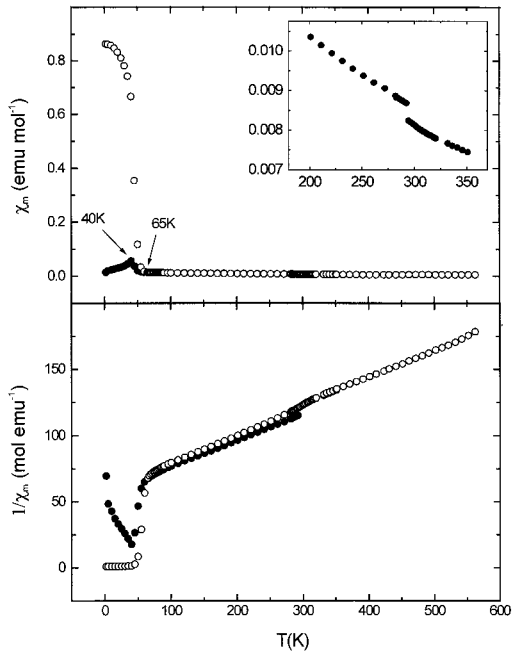

Figure 11. Direct currentsusceptibility and inverse susceptibility for $LiMn_2O_4$ as a function of temperature: (●) zero-field-cooled and (○) field-cooled measurements. The inset details the change in χ_{dc} at the Verwey transition.

DSC measurements on both samples are very similar. Both clearly show a reversible phase transition with an endothermic peak at 27.8 °C in the heating cycle and an exothermic peak at 8.2 °C in the cooling (Figure 10). This hysteresis is characteristic of a first-order phase transition and results in only partial conversion back to the cubic phase upon reheating the sample to room temperature. The latent heats of the phase transition, ΔH, may be estimated from the integrated area under the DSC peak and are found to be 5.7 and 6.0 J g^{-1} for heating and cooling cycles, respectively. These values are comparable with those previously reported.[10]

The dc susceptibility of both samples measured in 100 G was found to behave in the same manner. The susceptibility shows an abrupt jump at ~295 K (Figure 11), which corresponds to the Verwey transition, and the partial localization of the Mn^{3+} and Mn^{4+} ions. Upon cooling, a divergence between zero-field-cooled and field-cooled data is observed at ~65 K, below which the field-cooled data continue to rise until reaching a saturation value at ~5 K. For both samples the derivative $d(\chi T)/dT$ indicates that $T_c \sim 45$ K, at which temperature the zero-field-cooled data show a maximum.

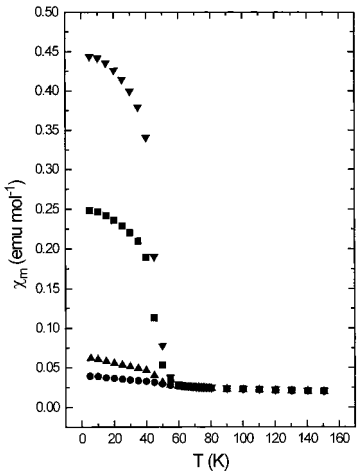

Figure 12. Field-cooled dc susceptibility for $LiMn_2O_4$ as a function of temperature in measuring fields: (●) 50 000 Oe, (□) 10 000 Oe, (■) 1 000 Oe, and (□) 500 Oe.

The 400−500 K data can be fitted to the Curie−Weiss law (eq 6) to yield values of the Curie constant and Weiss temperature of $C = 4.86(15)$ emu K mol^{-1} and $\theta_w = -300(20)$ K, respectively. The value of the Curie constant is consistent with Mn^{3+} being in the high-spin configuration and the average Mn valency, v(Mn), is 3.50(8).

$$\chi = C/(T - \theta_w) \quad (6)$$

Application of a large magnetic field is found to decrease the proportion of the canted spin phase and to suppress the transition at ~45 K, as demonstrated in Figure 12.

Central to the idea of frustration is that there is a depression of the ordering temperature, T_c, with respect to an upper limit defined by θ_w. Thus, a simple definition of a "frustration index", f, is given by[25]

$$f = |\theta_w|/T_c \quad (7)$$

However, care must be taken in the use of f as a sole criteria for frustration as it is influenced greatly by further neighbor interactions and dimensionality. In the case of $LiMn_2O_4$, the large negative value of the Weiss temperature, θ_w, indicates that there is strong antiferromagnetic exchange, and the lack of a transition in the dc susceptibility, once the moments are localized below 295 K until ~45 K demonstrates that this magnetic system is indeed frustrated, $f = 6.7$. Above this temperature, strong spin−spin correlations are still present, and these give rise to a separation of zfc and fc measurements in the susceptibility at ~65 K. Neutron diffraction directly examines these correlations and in addition to the scattering at low angles, a broad temperature-dependent diffuse feature centered at $q \approx 16.2$ $Å^{-1}$ (where $q = 2\pi/d$) is clearly observed in the data at 100 K, indicating the onset of short-range magnetic correlations. From the width of the feature the spin−

(25) Ramirez, A. P. *Annu. Rev. Mater. Sci.* **1994**, *24*, 453.

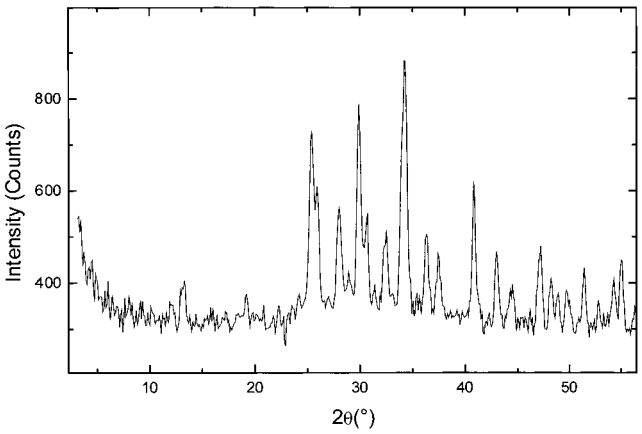

Figure 13. Low-angle region of neutron powder diffraction pattern from sample A of $LiMn_2O_4$ taken at 10 K with neutrons of wavelength 2.3713 Å.

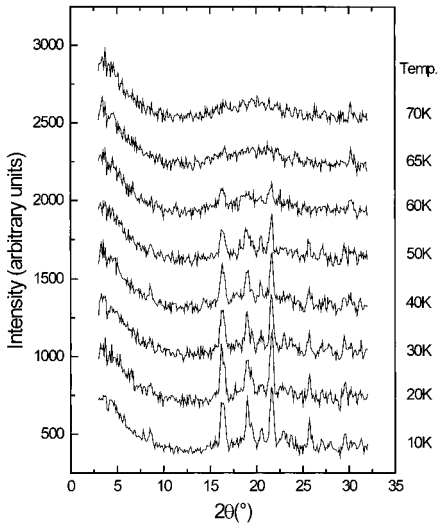

Figure 14. Powder neutron diffraction patterns of sample B of $LiMn_2O_4$ taken between 10 and 70 K with neutrons of wavelength 1.5030 Å.

spin correlation length can be estimated as ~2.3 Å. These correlations are therefore extended only between nearest-neighbor Mn atoms, d(Mn−Mn) ≈ 2.7 Å. Upon cooling below ~65 K new Bragg peaks at low angle are observed and these continue to evolve as the temperature is reduced (Figures 13 and 14). However, at 10 K diffuse scattering still persists which indicates that a significant fraction of the spins remain disordered even well below T_c. Furthermore, the peak width of the diffuse feature does not appear to change with temperature.

The appearance of the magnetic Bragg peaks at such low angles indicates that the magnetic cell is larger than the crystallographic and indeed they are found to index on a tetragonal cell which is 2a, 2b, 4c with respect to the tetragonal cell at 100 K. This large cell volume of ~40 327 Å^3, containing 1152 magnetic Mn atoms, greatly hinders any attempt to determine the magnetic structure, and indeed, given the high density of supercell reflections, one should regard even the assignment of the unit cell dimensions as tentative at this stage and not necessarily unique. The temperature dependence of the integrated intensity of one of the most intense magnetic reflections (at about 16.3°) for sample B, Figure 15, verifies that T_c is actually 65 K and not 45 K.

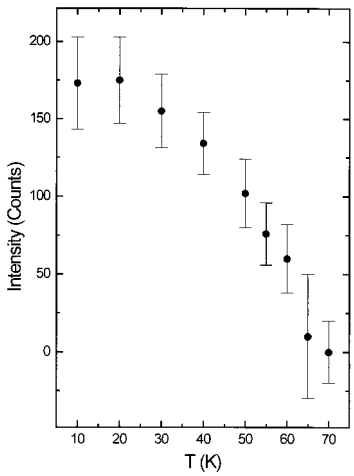

Figure 15. Integrated intensity of the feature centered at $2\theta = 16.3°$ as a function of temperature for sample B of $LiMn_2O_4$ taken with neutrons of wavelength 1.5030 Å.

4. Discussion

Rather than a continuous second-order structural transition, a first-order change is observed in the neutron diffraction pattern as the sample is cooled from room temperature. A Weiss temperature of 300 K suggests that short-ranged magnetic correlations will begin building up from room temperature, even in such a frustrated system. There is therefore a question regarding the origin of the progressive nature of the transition and whether it is due to a gradual increase in the magnetic correlations or a result of an activation energy associated with the tetragonal distortion. This question cannot be resolved without detailed examination of the extent of magnetic correlations up to T_v and such experiments are planned for the future.

For the spinel structure with a random distribution of Jahn−Teller active ions on the octahedral sites, Goodenough[26] demonstrated that the elastic energy of the crystal will be minimized when the tetragonal axes are parallel to one another. In the bulk lattice this produces an axial ratio $c/a > 1$. In the case of Mn_3O_4, where again Mn^{3+} is present as a Jahn−Teller active ion, this ratio is ~1.16. The tetragonal distortion in $LiMn_2O_4$ however is more complex than in Mn_3O_4 and leads to a far larger unit cell. However, a comparison is still useful and can be made in terms of the reduced tetragonal cell, i.e., with one-ninth of the volume of the 100 K unit cell, and using the relations 1 and 2 which yields the axial ratio $c/a = 0.993$. The somewhat surprising absence of a tetragonal elongation typically associated with Jahn−Teller systems indicates that the local distortions demanded by the charge-ordered fraction of Mn^{3+} can be accommodated without a cooperative effect, perhaps due to the incomplete nature of the segregation of the Jahn−Teller active ordered fraction.

Resistivity and thermopower measurements indicate that $LiMn_2O_4$ is a small polaron semiconductor and that the activation energy for electron hopping is in the range

(26) Goodenough, J. B.; Loeb, A. L. *Phys. Rev.* **1955**, *98*, 391.

0.16−0.39 eV. [8−10,27] This behavior is in contrast to the mixed-valent perovskite $La_{1-x}Sr_xMnO_3$, where $x \geq 0.2$, in which the e_g electron is delocalized and the materials are metallic. In $La_{1-x}Sr_xMnO_3$ the Mn ions share a common O 2p orbital and the Mn−O−Mn interactions are via an ∼180° bridge. The interaction is sufficiently strong to produce a conduction bandwidth suitable for itinerant e_g electrons. In $LiMn_2O_4$ the Mn−Mn magnetic interaction involves a 90° bridge which is less favorable for delocalization of e_g electrons and is thus believed to be too weak to lead to metallic behavior.[18,28]

The local Mn−O−Mn geometry in $LiMn_2O_4$ also has implications for the magnetic interactions which can be separated into several contributions. First, there is a superexchange pathway arising from the overlap of t_{2g} orbitals on Mn ions in adjacent edge-sharing octahedra, unmediated by oxide ion p orbitals. As the t_{2g} orbitals are half-filled for both high spin Mn^{3+} ($t_{2g}^3e_g^1$) and Mn^{4+} (t_{2g}^3), this interaction will be antiferromagnetic. In addition, there will be 90° Mn−O−Mn interactions. As the Mn^{3+} and Mn^{4+} ions are completely disordered above the Verwey transition at 10 °C and remain at least partially disordered in the low-temperature structure, all three possibilities 90° Mn^{4+}−O−Mn^{4+}, Mn^{4+}−O−Mn^{3+}, and Mn^{3+}−O−Mn^{3+}, will be present. It has been argued that the former will be ferromagnetic and the latter two interactions, antiferromagnet. [26]

Comparison of $LiMn_2O_4$ with the cubic spinel, λ-MnO_2, allows an assessment of the relative importance of the various contributions to the Mn−Mn magnetic exchange, as at room temperature the two materials are isostructural. The sample of λ-MnO_2 studied previously[16] contained at least 90% Mn^{4+} and has a correspondingly smaller unit cell dimension and shorter Mn−Mn distance than $LiMn_2O_4$ and thus, one expects, a stronger t_{2g}−t_{2g} interaction. Nonetheless, θ_w is more negative in $LiMn_2O_4$ by a factor of 3, −300 to −104 K. In λ-MnO_2, one has only, or for the current sample, predominantly, the competing antiferromagnetic t_{2g}−t_{2g} and ferromagnetic Mn^{4+}−O−Mn^{4+} 90° pathways. While both of these pathways are still present in $LiMn_2O_4$ the additional antiferromagnetic pathways, 90° Mn^{4+}−O−Mn^{3+} and Mn^{3+}−O−Mn^{3+}, will also be important and thus, the more negative θ_w relative to λ-MnO_2 can be understood, at least semiquantitatively.

The large magnetic unit cell apparent from the neutron powder diffraction data below 60 K is compatible with the two ideas that there is a partial ordering of charges and that frustration leads to a large number of groundstates. What is perhaps of interest is that the magnetic cell appears to be based on a cubic structure and there is the possibility that the magnetic structure is based on, or has some similarities, with those of other cubic spinel systems and indeed with that observed in the lithium depleted λ-MnO_2.[16]

The geometric frustration associated with the magnetic pyrochlore sublattice is manifested in the depression of the T_c with respect to the value of θ_w, and above T_c in the deviation of the susceptibility from the Curie−Weiss law up to ∼350 K. In this temperature region, short-range correlations between the spins cause divergence away from the simple description of a paramagnet. The temperature range over which this occurs, up to $7T_c$, is extended far beyond that of more conventional unfrustrated systems, and demonstrates well the difficulty that the magnetic system has to order. It is perhaps surprising that despite the presence of partial Mn^{3+}/Mn^{4+} site disorder and a geometrically frustrated Mn lattice, a spin glasslike ground state is not selected for $LiMn_2O_4$, but instead a long-range ordered state emerges, albeit one of extraordinary complexity which coexists with short-range order down to the lowest temperatures examined, 10 K.

The apparent contradiction in the literature concerning the presence or absence of an antiferromagnetic transition at low temperature is easily resolved by the observed suppression of the transition by the application of a large magnetic field. Reported data were often collected in fields of 10 000[17] and 50 000 Oe[8] and under these conditions any change in the magnetic response at the transition will be considerably lessened as demonstrated in Figure 12. Variation of the magnetic responses with precise sample stoichiometry is also expected.

At the Verwey transition, T_v, the structural changes associated with the partial localization of the e_g electrons implied by the formation of distinct Mn^{3+} and Mn^{4+} sites should be reflected in the electron transport and paramagnetic susceptibility. Perhaps remarkably, the dc susceptibility shows only a small anomaly at the transition in $LiMn_2O_4$, Figure 11, and the resistivity increases by only an order of magnitude.[8] These relatively minor anomalies are a consequence of the weakness of the Mn−Mn interactions. Above T_v, the electron-hopping model already involves a contribution from static e_g electrons and as a consequence, any changes upon localization are therefore small.[29]

5. Summary

The structural phase transition in $LiMn_2O_4$ at room temperature has been examined using powder neutron diffraction. A large tetragonal cell is proposed to describe the low-temperature structure in space group $I4_1/amd$. Bond-valence calculations around the Mn environments are consistent with partial segregation of the Mn^{3+} and Mn^{4+} species, with Mn^{4+} being preferentially located at higher symmetry 8d sites. The transition is associated with partial localization of e_g electrons and the formation of distinguishable Mn^{4+} and the Jahn−Teller active Mn^{3+} species. The somewhat surprising absence of an axial elongation typically associated with cooperative Jahn−Teller systems is attributed to the ability of the low-temperature structure to accommodate the distortions associated with the charge ordered fraction of Mn^{3+} ions without a cooperative effect and to the relatively low concentration of these sites. Direct current susceptibility measurements show a separation of field-cooled and zero-field-cooled measurements at ∼65 K below which powder neutron diffraction shows the presence of magnetic long-range order. The mag-

(27) Schütte, L.; Colsmann, G.; Reuter, B. *J. Solid State Chem.* **1979**, *27*, 227.
(28) Goodenough, J. B.; Manthiram, A.; Wnetrzewski, B. *J. Power Sources* **1993**, *43*−*44*, 269.
(29) Sugiyama, J.; Tamura, T.; Yamauchi, H. *J. Phys. Condens. Matter* **1995**, *7*, 9755.

netic Bragg peaks index on a tetragonal cell with the ordering vector $\mathbf{k} = (^1/_2\ ^1/_2\ ^1/_4)$ which contains 1152 Mn spins. Such a large magnetic unit cell and the implied complexity of the magnetic structure is consistent with both charge segregation and the stabilization of complex canted spin arrangements by further neighbor interactions in the spinel structure. The coexistence of diffuse scattering along with the Bragg peaks shows also that a significant fraction of spins remain disordered at 10 K.

6. Acknowledgments

J.E.G. is supported by the Natural Sciences and Engineering Research Council of Canada. We would like to thank Drs. Zin Tun and Ian Swainson, and Ron Donaberger for assistance with the neutron scattering experiments at the Chalk River Nuclear laboratories; and C. Masquelier for the communication of their results prior to publication.

CM981041L